David Tomás Sánchez Martínez
Lourdes García Rodríguez
(coordinadores)

Proceedings of the 7th International Seminar on ORC Power Systems

Editorial Universidad de Sevilla

Proceedings of the 7th International Seminar on

ORC
Power Systems

David Tomás Sánchez Martínez
Lourdes García Rodríguez
(coordinadores)

Proceedings of the 7th International Seminar on

ORC Power Systems

(ORC2023)

4th to 6th
SEPTEMBER
SEVILLE 2023

EDITORIAL UNIVERSIDAD DE SEVILLA

Sevilla, 2024

Colección Actas
Núm.: 91

Review chairs of the 7th International Seminar on ORC Power Systems

Prof. Christoph Wieland (University of Duisburg-Essen) - *Review Chair*
Prof. Sotirios Karellas (National Technical University of Athens) - *Review Co-Chair*
Prof. Teemu Turunen-Saaresti (LUT University) - *Review Co-Chair*
Dr. Diego-César Alarcón-Padilla (Plataforma Solar de Almería - CIEMAT) - *Review Co-Chair*
Dr. Francesco Crespi (Universidad de Sevilla) - *Review Co-Chair*

ISBN 978-84-472-2745-7
DOI: https://dx.doi.org/10.12795/9788447227457

Diseño de cubierta y maquetación: los autores

INDEX OF CONTRIBUTIONS

DOI: https://dx.doi.org/10.12795/9788447227457_16

SHAPE OPTIMIZATION OF A sCO_2 CENTRIFUGAL COMPRESSOR STAGE

Alessandro Romei*, Paolo Gaetani, Giacomo Persico

Laboratory of Fluid Machines,
Department of Energy, Politecnico di Milano,
Via Lambruschini 4a, 20156 Milano, Italy
*Corresponding Author: alessandro.romei@polimi.it

ABSTRACT

The design of a centrifugal compressor for supercritical carbon dioxide (sCO_2) power cycle must account for non-ideal gas effects and the possible occurrence of two-phase flows. Shape optimization techniques combined with computational fluid-dynamic (CFD) simulations can produce optimized designs while inherently coping with the peculiar flow characteristics near the thermodynamic critical point.

This work presents the first shape-optimization attempt of such non-conventional compressors. The compressor stage includes the impeller and the vaneless diffuser and starts the compression close to the critical point. The impeller blade angle distributions and meridional channel are parameterized with Bezier control points, which grant a local shape control within the optimization routine. The pinch of the vaneless diffuser is optimized as well. The validated CFD solver accounts for both non-ideal effects and two-phase homogeneous flows under the assumption of thermodynamic equilibrium and barotropic fluid. The constrained optimization problem is solved with genetic algorithms. To reduce the computational cost, surrogates for the objective function and constraints are trained over a limited number of CFD results. The surrogate accuracy is improved throughout the optimization process by adding optimal stage geometries to the initial training samples.

The optimized geometry shows an appreciable efficiency increase (0.7 percentage points) while delivering the design pressure ratio. Although performing better in the design condition, the operating range of the compressor is altered by optimization. This finding leaves the door open for future optimizations that include both design and off-design operating points in the definition of the objective function and constraints.

1 INTRODUCTION

The use of carbon dioxide operating in thermodynamic supercritical conditions (sCO_2) as working fluid in closed gas cycles offers the opportunity to exploit multiple classes of hot sources alternative to fossil fuels, ranging from nuclear energy to concentrated solar power and waste heat from industrial processes, owing to the expected higher efficiency and smaller plant footprint with respect to conventional configurations such as steam or organic Rankine cycles. Moreover, sCO_2 power systems also benefit from compactness, thanks to the high density of the working fluid, which ultimately offers the opportunity for effective control of the dynamics of the plant.

A key component of sCO_2 power systems is the main compressor, which is usually centrifugal due to the typical low volumetric flow rates and operates close to the thermodynamic critical point. The corresponding compression process allows for a significant reduction of the work required thanks to the liquid-like properties of CO_2 in these thermodynamic conditions. However, the large departure from the ideal-gas thermodynamics (Pecnik et al., 2012; Baltadjiev et al., 2015; Ameli et al., 2018), as well as the potential occurrence of two-phase flows (Lettieri et al., 2015; Hosangadi et al., 2019; Persico et al., 2021), pose challenges in the aerodynamic design of impeller blade and meridional channel. The set-up of reliable design tools that comply with the above non-ideal effects is crucial to accelerate the development and the success of the entire technology.

Most of the studies available in the literature analyze the aerodynamics and thermodynamics of the flow within the machine or discuss the validation of computational tools for compressor flow analysis. However, few works (see, for example, Pelton et al., 2017) focus on the design process of such non-conventional machines. In the present study, we propose automatic shape optimizations as a means to design sCO_2 centrifugal compressors. Leveraging a validated computational fluid-dynamic (CFD) solver, which provides an accurate representation of thermophysical fluid properties and accounts for the onset of two-phase flows, shape optimization has the potential to unveil new design paradigms for sCO_2 compressor stages.

2 BASELINE GEOMETRY

The baseline machine is a single-stage centrifugal compressor that was designed from scratch for the inlet total conditions of $P_{01} = 85\ bar$ and $T_{01} = 305\ K$ and has to provide an outlet pressure of $250\ bar$. The compressor stage includes a shrouded impeller and a vaneless diffuser. The main design parameters are: $\phi_{01} = 0.04$, $\phi_2 = 0.20$, $M_u = 0.70$, and $\lambda = 0.625$. The impeller has 8 main blades and 8 splitter blades resulting from blade loading considerations. The meridional channel, the blade angle distribution, and the thickness distribution for the main impeller blades are reported in Figure 1. The splitter blade is obtained by cutting the blade angle distributions at a specified normalized meridional coordinate $\tilde{m}$ and applying the same thickness distribution as the main blade. The splitter for the baseline geometry starts from $\tilde{m} = 0.2$.

102

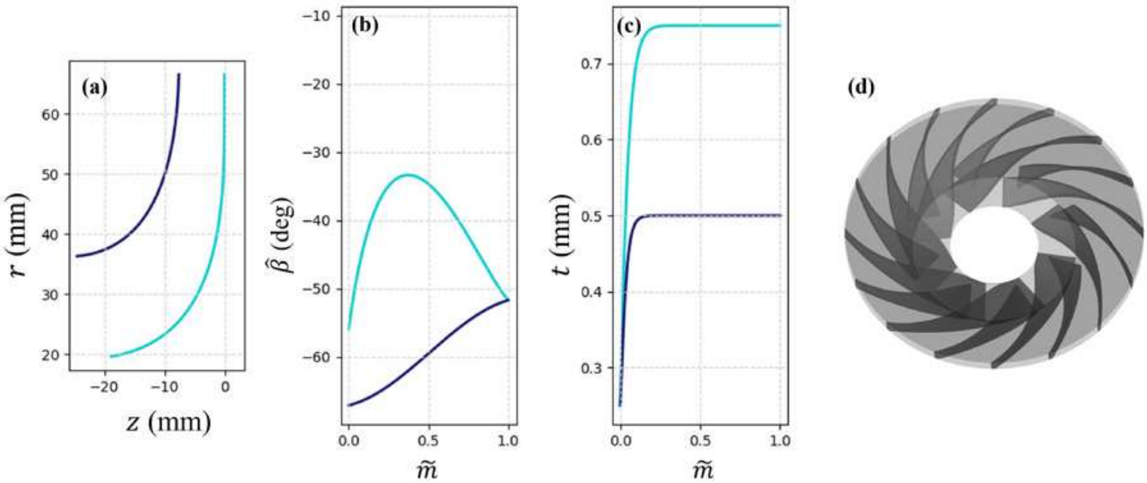

Figure 1: Baseline impeller geometry. (a) meridional view. (b) blade angle distribution. (c) thickness distribution. (d) three-dimensional view.

The performance estimates are determined based on steady RANS simulations. The RANS equations are solved with the Ansys-CFX finite-volume flow solver, using high-order numerical schemes for both inviscid and viscous fluxes. Turbulence effects are introduced by resorting to the $k-\omega$ SST model assuming a fully turbulent flow.

A specific feature of the present model refers to the representation of the non-ideal thermodynamics of the fluid. This is crucial for the proper modeling of turbomachinery operating with sCO_2, whereby the proximity to the critical point originates a large departure from ideal-gas behavior. In particular, the thermodynamic description of the fluid is modeled here by resorting to the Span-Wagner equation of state. However, the challenges of simulating the flow in technically-relevant sCO_2 compressors are also related to two-phase flows: the proximity of the inlet compressor state to saturation might indeed trigger phase change processes that need to be taken into account in the simulation model. In this work, we make use of a barotropic model, which belongs to the class of homogeneous equilibrium models (HEM), in which the thermo-physical properties (density and dynamic viscosity) of the fluid are assumed only depending on pressure. The barotropic relationships $\rho = \rho(P)$ and $\mu = \mu(P)$ are generated along the isentrope at the impeller inlet section for each thermodynamic state. The barotropic model was first proposed for application to sCO_2 compressors by the same authors (Persico et al., 2021), and it was subsequentially validated against experimental data of a MW-scale sCO_2 centrifugal compressor prototype by Toni et al. (2022).

The computational mesh was generated with Ansys-Turbogrid. To reduce the computational cost per simulation, which is critical in shape optimization tasks, periodic boundary conditions are exploited. Therefore, the computational domain includes a single-blade passage containing the main blade, the splitter blade, and the vaneless diffuser. Other components, such as the volute and the sealings, are omitted to limit the computational cost. After a grid-dependence analysis, a mesh composed of 1.7 million cells was adopted. The resulting grid convergence index for the total-to-total efficiency η_{TT} is 0.3%.

Calculations were performed assigning the total state at the inlet. The flow rate was imposed at the outflow, except close to choked-flow conditions, for which an average static pressure was assigned. No-slip boundary conditions were imposed on the solid walls. As the flow domain is rotating with the impeller, a counter-rotating velocity was assigned at the endwalls of the vaneless diffuser. Considering the high Reynolds number ($\sim 10^8$) as a consequence of the low kinematic viscosity of carbon dioxide in supercritical conditions, the assumption of hydraulically smooth surfaces is not appropriate and, hence, wall roughness ($k_s = 5\ \mu m$) and corresponding wall functions are specified.

The CFD simulation returns a $\eta_{TT} = 92.2\%$, $\lambda = 0.625$, and an outlet total pressure of $266\ bar$. This value of total pressure is sufficient to meet the cycle target of 250 bar while accounting for the losses in additional components (e.g., volute) and the dissipation of the residual kinetic energy.

3 SHAPE OPTIMIZATION

3.1 Shape parameterization

To perform the shape optimization, the baseline geometry needs to be parameterized with a finite number of control points, which becomes the design variables. This task is accomplished by parameterizing the meridional channel and the blade angle distribution with Bezier control points as in Figure 2. Four control points are used to reproduce the meridional hub contour $\{M_{hj}\}$, the meridional shroud contour $\{M_{sj}\}$, the hub blade angle distribution $\{B_{hj}\}$, and the shroud blade angle distribution $\{B_{sj}\}$, with $j = 1, \dots, 4$. Not all these design parameters are independent: (i) the trailing edge is cut at the same radial coordinate, therefore the last control point of the hub contour follows the displacement of M_{s4}, and (ii) the outlet blade angle does not change along the span, hence a single control point B_4 is considered for both the hub and the shroud distribution. The thickness distribution is not modified throughout the optimization not to compromise the mechanical integrity of the impeller. In general, the splitter blade may follow a different blade angle distribution with respect to the main blade; however, to reduce the number of design variables, the splitter follows the main blade distributions, and the only design parameter is the meridional coordinate at which the main blade is cut (S). Finally, a front-pinch is considered for the vaneless diffuser, and the diffuser pinch (ζ) and the radial coordinate at which the straight part begins (δ) can be both objects of the optimization. The vaneless diffuser extends up to $R_3 = 1.6\ R_2$.

Overall, 17 design variables are considered for the shape optimization problem, of which 7 are related to the meridional channel, 7 control the blade angle distribution, 2 parameterize the vaneless diffuser, and 1 is for the splitter. Table 1 reports the design space for each of these design variables.

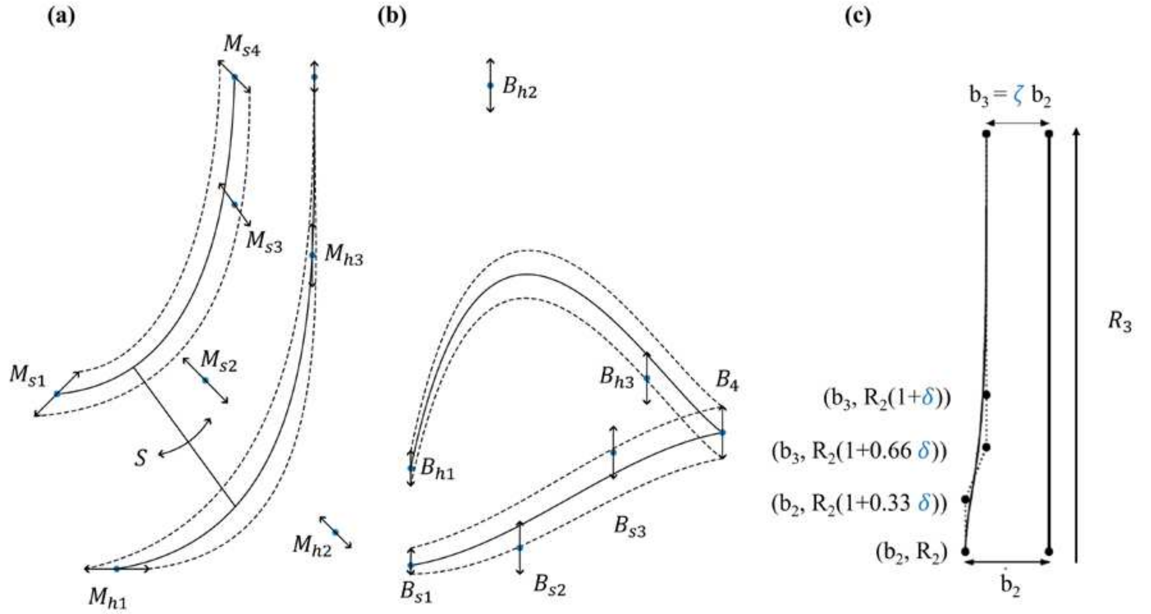

Figure 2: Centrifugal compressor stage parameterization. (a) meridional channel. (b) blade angle distribution. (c) vaneless diffuser.

Table 1: Design space identified by 17 design variables.

	M_{h1}	M_{h2}	M_{h3}	M_{s1}	M_{s2}	M_{s3}	M_{s4}	S	
Max	3.0 mm	2.0 mm	3.0 mm	3.0 mm	3.0 mm	2.0 mm	2.0 mm	0.45	
Min	-3.0 mm	-2.0 mm	-3.0 mm	-3.0 mm	-3.0 mm	-2.0 mm	-2.0 mm	0.15	
	B_{h1}	B_{h2}	B_{h3}	B_{s1}	B_{s2}	B_{s3}	B_4	δ	ζ
Max	2.0 deg	3.0 deg	3.0 deg	2.0 deg	3.0 deg	3.0 deg	3.0 deg	0.20	1.00
Min	-2.0 deg	-3.0 deg	-3.0 deg	-1.0 deg	-3.0 deg	-3.0 deg	-3.0 deg	0.10	0.60

104

3.2 Surrogate-assisted evolutionary strategy

The optimization problem aims at maximizing the total-total efficiency η_{TT} of the stage. Moreover, three constraints are considered, involving the work coefficient λ, the absolute flow angle α_3 at $1.2R_2$, and the mass imbalance $\dot{m}_{imb}$ of the solution. The first two constraints follow aerodynamic consideration. The work coefficient is constrained because the optimal compressor has to provide the required pressure ratio. The absolute flow angle cannot exceed 67 deg (measured from the meridional direction) to keep a safe margin from the onset of instabilities in the vaneless diffuser thus guaranteeing a wide operating range. The last constraint about the mass imbalance is included explicitly in the optimization routine to discard solutions that are characterized by a bad convergence. Therefore, the optimization problem reads as:

$$\max \quad \eta_{TT} \tag{1.1}$$
$$s.t. \quad 0.62 \leq \lambda \leq 0.63 \tag{1.2}$$
$$60\ deg \leq \alpha_3 \leq 67\ deg \tag{1.3}$$
$$|\dot{m}_{imb}| \leq 0.1\% \tag{1.4}$$

The constrained optimization problem is solved with the genetic algorithm (GA). As the GA requires many evaluations to converge, a surrogate strategy is adopted to reduce the computational cost, leveraging the surrogate-assisted strategy implemented in the in-house optimizer FORMA (Persico et al., 2019).

Figure 3 summarizes the optimization workflow. At first, 170 stage geometries are generated within the prescribed design space with Latin hypercube sampling. The objective function and the constraints are calculated with CFD simulations as detailed in section 2. The mesh is regenerated each time using the grid-convergent set-up described before. Four distinct Kriging, one for each objective function/constraint, are introduced as surrogates of the CFD simulation. The employed Kriging models have up to second-order monomials of the input variables as the mean trend and incorporate a Gaussian correlation function. The Kriging hyperparameters are determined by maximum likelihood estimation.

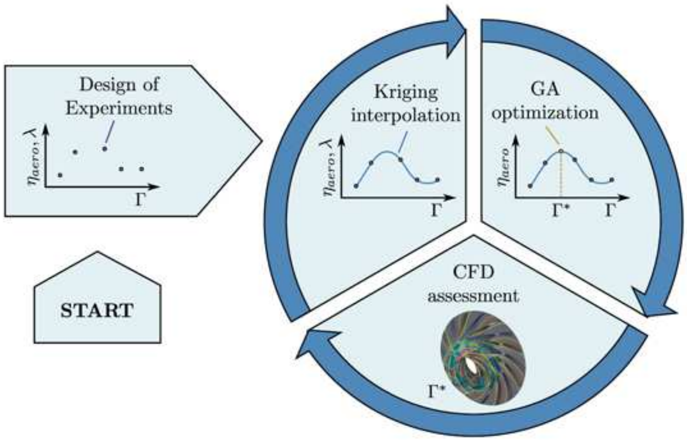

Figure 3: Flow chart summarizing the surrogate-assisted shape optimization strategy.

Once the four Kriging predictors are obtained, the GA optimization is executed on surrogate responses. The so-identified optimal stage geometry is assessed with CFD, and new Kriging predictors are re-generated on all simulated cases, namely the initial design of experiments plus the simulated optimal geometries selected by the surrogate optimization. In this way, the surrogate reliability progressively increases by adding geometries close to the expected optimal region. The optimization procedure is repeated until convergence, i.e. the surrogate optimization converges to the same optimal geometry of the previous iteration.

3.3 Optimal geometry

The convergence history of the optimization is shown in Figure 4. It reports the convergence after the first surrogate training on the design of experiments obtained with Latin hypercube sampling. In the initial design pool, there are no geometries that can outperform the baseline while satisfying all the constraints. Looking at the convergence history, the mass imbalance does not affect the convergence process. Except for a few solutions, most of the simulations have negligible values of mass imbalance between the inlet and the outlet section. Meeting the targets for λ and α_3 is more critical, especially the latter. Apparently, the best efficiency is obtained for absolute flow leaving the impeller with a more tangential direction. The optimal solutions are found close to the upper limit of the α_3-constraint (67 deg). The increase in the absolute flow angle will have a detrimental effect on the machine operation at low flow rates (left limit of the operating curve). As a result, the optimal compressor stage shows a $\eta_{TT} = 92.9\%$, with an increase of 0.7 percentage points from the baseline value, while satisfying the imposed aerodynamics constraint, namely $\lambda = 0.629$ and $\alpha_3 = 66.7\ deg$.

Figure 5 compares the baseline and the optimal impeller geometries. The main changes in the meridional channel are localized at the hub, whose curvature is slightly increased. Then, the backswept of the blade is reduced, shifting the entire shroud blade angle distribution to more meridional values. Moreover, the splitter length is increased to further reduce the aerodynamic loading in the front part of the blade, which has been increased as a consequence of the higher work coefficient. At the same time the splitter length does not increase the blockage in the impeller inlet area to prevent the onset of choking. It is interesting to note that the optimization has changed the front part of the shroud blade profile, which is typically the most critical region where most of the diffusion occurs. In this region, there is also a two-phase supersonic pocket, as highlighted in Figure 6 by the sudden increase in the Mach number. This two-phase region is slightly increased for the optimal stage because of the positive incidence that results from a more meridional inlet blade angle. However, in this way, the flow detachement on the blade suction side is considerably reduced, motivating the path followed by the optimization to increase the total-total efficiency.

The complete list of optimal design variables is reported in Table 2. From this table, it can also be observed that the optimal stage has a vaneless diffuser with a pinched section that extends up to $1.18\ R_2$ and reduces the outlet blade height by almost 20%. Interestingly, the optimal values for some variables are found at the extreme boundary of the associated design space, suggesting that there may be space for further improvement by enlarging the design space. In particular, the shroud blade angle distribution would shift to a more meridional direction.

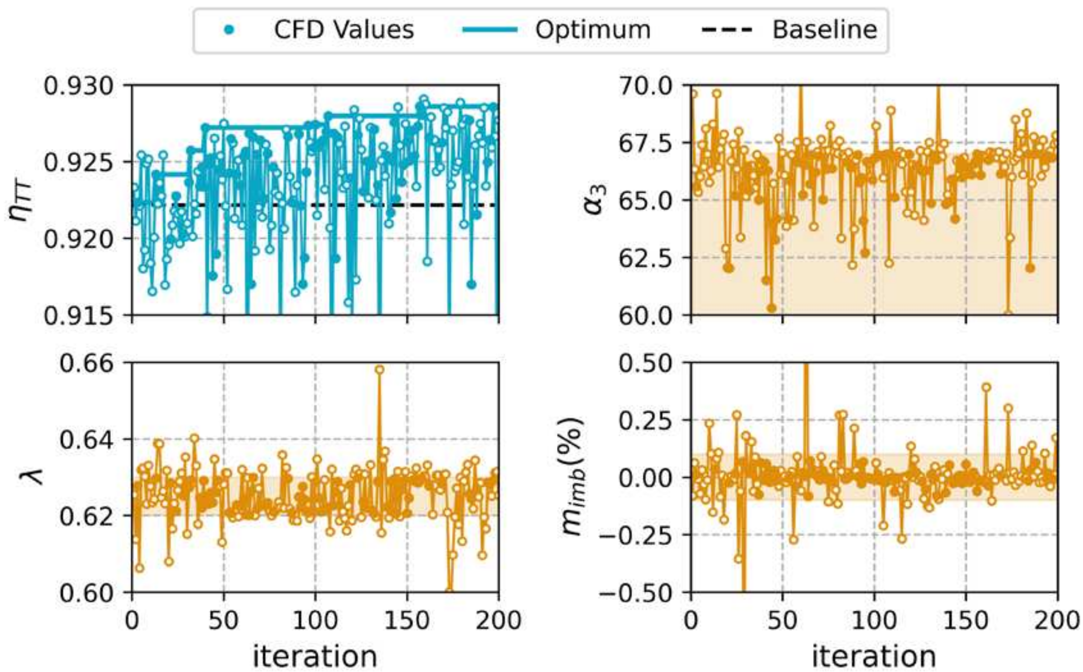

Figure 4: Convergence history. The filled mark indicates a geometry that satisfies all constraints. The void mark indicates a geometry for which at least one constraint is not satisfied.

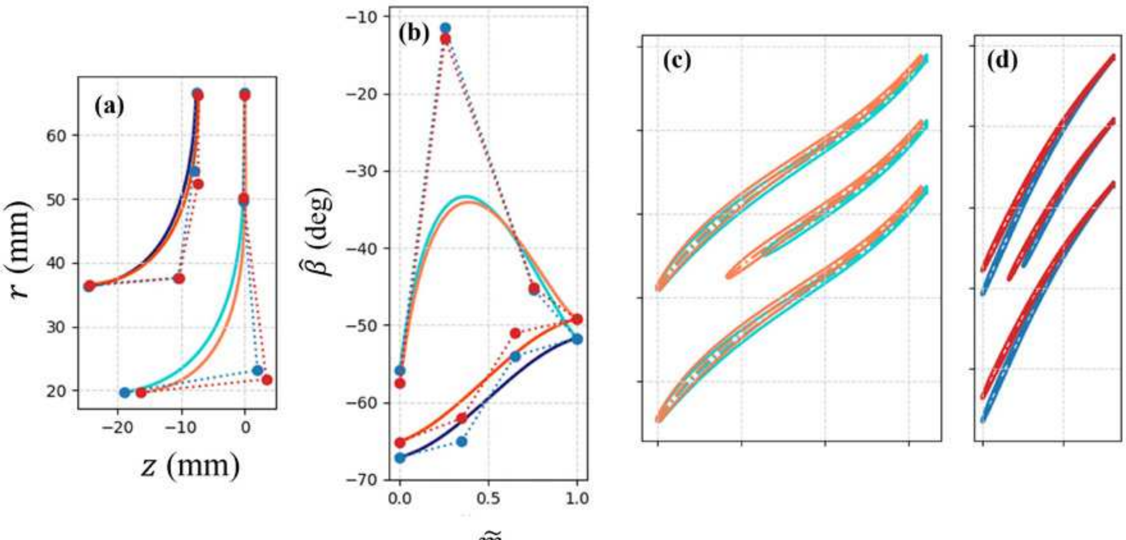

Figure 5: Baseline (cyan/blue) and Optimal (red/orange) impeller geometries. (a) meridional view. (b) blade angle distribution. (c) blade-to-blade view at hub. (d) blade-to-blade view at tip.

106

Table 2: Optimal design variables. Variables marked with * means that the optimal solution is found at the boundary of the associated design space.

	M_{h1}	M_{h2}*	M_{h3}	M_{s1}	M_{s2}	M_{s3}	M_{s4}	S	
Opt	2.6 mm	2.0 mm	0.6 mm	0.3 mm	-0.1 mm	-1.9 mm	-0.5 mm	0.16	
	B_{h1}	B_{h2}	B_{h3}	B_{s1}*	B_{s2}*	B_{s3}*	B_4	δ	ζ
Opt	-1.6 deg	-1.3 deg	2.5 deg	2 deg	3 deg	3 deg	2.5 deg	0.18	0.79

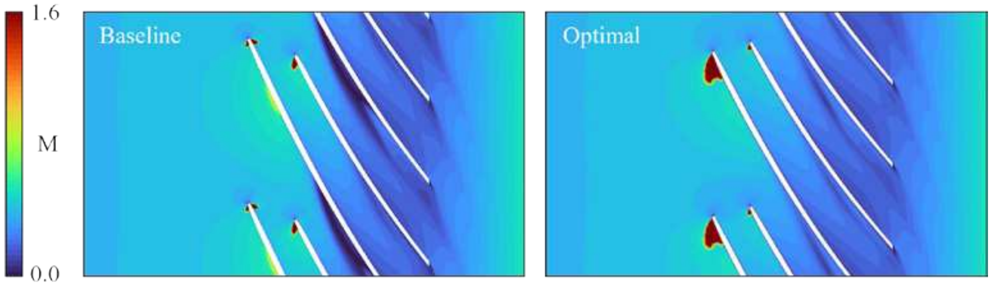

Figure 6: Mach number fields at tip section (90% blade height) for baseline and optimal stages.

As the last analysis, it is worth investigating the variation in the operating range after the optimization. The performance map across the flow range at the nominal rotational speed is reported in Figure 7. Both the right and the left limits are changed as a result of the optimization.

On the one hand, the left limit, which identifies the minimum mass flow rate without incurring compressor instability, is moved towards a higher flow rate in the optimized case by almost 10%. This increase in minimum flow rate can be explained in light of the higher work coefficient, which requires a larger flow diffusion. It is worth highlighting that the identification of the left limit with RANS simulations is not accurate, as the instabilities are inherently time-dependent phenomena and also depend on the machine-plant interaction. For the present analysis, the limit was set based on numerical consideration, i.e. when the simulation is not able to converge to a steady solution (oscillations in torque larger than 2%). 107

On the other hand, the right limit, which identifies the maximum mass flow rate before choked-flow conditions, is increased by 8%. As discussed in previous works (Persico et al. 2021; Toni et al., 2022), sCO_2 compressors are prone to an anticipated choking due to the sudden drop in the speed of sound for the two-phase flow mixture The choked-flow conditions occur similarly between the baseline and the optimal. The larger swallowing capacity of the compressor is a result of the larger flow passage area at the throat given by the hub curvature increase.

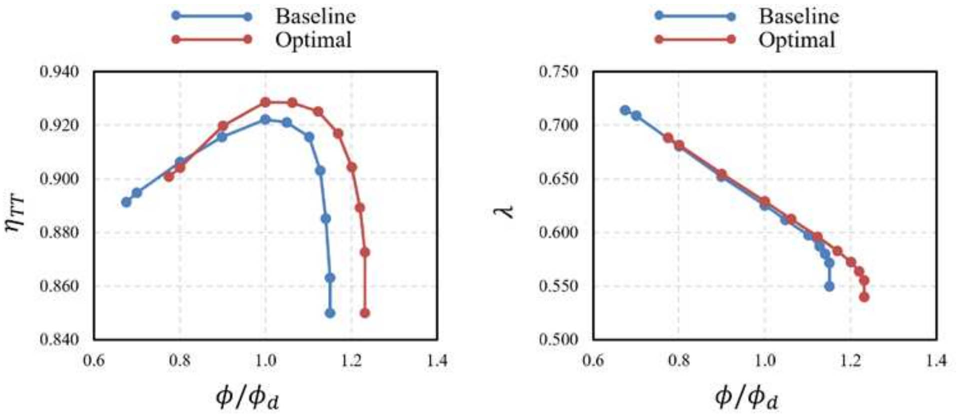

Figure 7: Efficiency (left) and work coefficient (right) curves over the flow range for baseline and optimized stage geometries.

4 CONCLUSION

This work discusses a first shape-optimization attempt for sCO_2 centrifugal compressor stage. The baseline stage is a single stage that provides an overall pressure ratio of about 3 starting from the upstream total conditions $P_{01} = 85\ bar$ and $T_{01} = 305\ K$. The baseline shape is parametrized with a number of Bezier curves for the meridional contours and the blade angle distributions. The geometrical parameterization also includes the length and the extent of the vaneless diffuser pinch and the initial splitter meridional location for a total of 17 design variables.

The shape optimization method is applied to optimize the baseline total-total efficiency while constraining the work coefficient and the absolute flow angle at the impeller outlet. The optimization converges to a new compressor shape that is more efficient (+0.7 percentage points in total-total efficiency) and satisfies the imposed constraints. As a side effect, the operating range of the compressor changes, with a reduction in the surge margin and an increase in the right limit. This finding leaves the door open for future optimizations that include both design and off-design operating points in the definition of the objective function and constraints.

REFERENCES

Ameli, A., Afzalifar, A., Turunen-Saaresti, T., and Backman, J., 2019, “Centrifugal compressor design for near-critical point Applications”. J Eng Gas Turbines Power 141 (3).

Baltadjiev, N. D., Lettieri, C., and Spakovszky, Z. S., 2015. “An Investigation of Real Gas Effects in Supercritical CO_2 Centrifugal Compressors”. J. Turbomach 137(9), 09.

Hosangadi, A., Liu, Z., Weathers, T., Ahuja, V., and Busby, J., 2019, “Modeling multiphase effects in CO_2 compressors at subcritical inlet conditions”. J Eng Gas Turbines Power 2019;141(8):081005.

Lettieri, C., Yang, D., and Spakovszky, Z., 2015. “An Investigation of Condensation Effects in Supercritical Carbon Dioxide Compressors”. J Eng Gas Turbines Power 137(8).

Pecnik, R., Rinaldi, E., and Colonna, P., 2012, “Computational fluid dynamics of a radial compressor operating with supercritical CO_2”, J Eng Gas Turbines Power 134 (12).

Pelton, R., Jung, S., Allison, T., and Smith, N., 2018. “Design of a wide-range centrifugal compressor stage for supercritical CO_2 power cycles”. J Eng Gas Turbines Power 140(9), 092602.

Persico, G., Gaetani, P., Romei, A., Toni, L., Bellobuono, E.F., and Valente, R., 2020, “Implications of phase change on the aerodynamics of centrifugal compressors for supercritical carbon dioxide applications”. J Eng Gas Turbines Power 143 (4).

Persico, G., Rodriguez-Fernandez, P., and Romei, A., 2020, “High-fidelity shape optimization of non-conventional turbomachinery by surrogate evolutionary strategies”. J. Turbomach. 141(8), 081010.

Toni, L., Bellobuono, E. F., Valente, R., Persico, G., Romei, A., and Gaetani, P., 2022. “Computational and Experimental Assessment of a MW-Scale Supercritical CO_2 Compressor Operating in Multiple Near-Critical Conditions”. J Eng Gas Turbines Power 144(10), 101015.

ACKNOWLEDGEMENT

The shape optimization workflow applied to centrifugal compressors has been developed in the framework of the CO2OLHEAT project, which has received funding from the European Union’s Horizon 2020 research and innovation programme under grant agreement N° 101022831.

This book contains the compilation of works contributed to the *7th International Seminar on Organic Rankine Cycle Power Systems* (ORC 2023), held in Seville between the 4th and 6th of September 2023. The event was hosted by Universidad de Sevilla on behalf of the Knowledge Centre on Organic Rankine Cycle Technology (KCORC), incorporated in The Netherlands.

The ORC conference, organized biennially, stems as the only conference that is specific to ORC technology, therefore gathering a diverse community whose affiliation spans across all the interested stakeholders, not only in this particular technology but also and in a broader context, in the energy transition. Original equipment manufacturers, professional associations, end-users, investors, policy makers, academics, scientists feel at home at ORC 2023.

The almost 100 proceedings in this book cover a wide variety of topics, from fundamentals to system integration through component design, accounting for thermodynamic performance as well as component design. In addition to this, and as a new track in 2023, works on heat pump technology were also accepted in order to raise awareness of the strong ties between both technologies, specifically in energy storage applications.

This book provides an excellent overview of the current maturity of power systems based on Organic Rankine Cycle technology for applications as diverse as geothermal and waste heat recovery in industry or downstream of other prime movers (e.g., marine applications). It is also an excellent source of information to understand the current challenges faced by the technology, stemming from a very competitive market and increasingly stringent environmental regulations.

The organizers of ORC 2023 hope that the reader finds this work as exciting as the attendees to the conference and, maybe, make the decision to join the 8th edition to the conference in 2025.

KCORC
KNOWLEDGE CENTER
ORGANIC RANKINE CYCLE

eus EDITORIAL
UNIVERSIDAD DE SEVILLA